

Chapter 5

Detection and Characterisation of rotational spherical aggregate rotational dynamics

As outlined in the end of Chapter 4, one of the difficulties in characterising interactions with asymmetric objects is the coupled motion between translation and rotation. This can be somewhat ignored if the rotational motion is periodic, like when the power spectra of elliptical polystyrene particles was fitted by Yogesh *et al* [1], however in the case where rotational motion is stochastic the problem is more complex. For example, when a novel trap characterisation technique was implemented by Saffron *et al* [2, 3], they were able to use dynamic light scattering to characterise both the axial and lateral trap stiffness acting on microspheres. The only drawback admitted to in their work was that the technique was constrained to isotropic scatters as their theoretical model for describing the auto-correlation function was predicated on the fact that any variations in the signal are due to the particles translational motion within the confines of a cylindrical trap [2]. However, it is somewhat naive to assume that the orientational change

5.1 Simulative QPD

A QPD is simply a measure of the total electric field incident on a photo diode, in order to accurately simulate a QPD response careful consideration of how the Electromagnetic fields are defined is required.

5.1.1 Incident beam

The incident beam is simple enough to define given our set up parameters, for the sake of simplicity we assume that our beam is a Laguerre-Gaussian beam of mode $[0.0, 0.0]$ (which is simply a pure Gaussian beam). *Ott* uses a point matching approach to approximate the beam shape coefficients of the incident field by fitting it to the far field estimate, the beam is of the form:

$$E_{inc}(kr) = \sum_n \sum_{m=-n}^n a_{mn} RgM_{nm}(kr) + b_{nm} RgN_{nm}(kr) \quad (5.1)$$

Where $RgM_{nm}(kr)$ & $RgN_{nm}(kr)$ are regular vector spherical wave functions, *ott* allows us to change the basis of the the incident beam to suit our needs, because we are measuring in the far field we want to set our incident beam to be an outgoing spherical wave so that we can compute the intensity on the QPD. For spherical waves the field can either be expressed as an incoming/outgoing wave (with a singularity at the origin) or as a regular wave around the origin; for incoming/outgoing waves the wave functions use the first/second forms of the Hankel function respectfully. In order to compute the regular spherical wave at the origin we replace the Hankel function with the Bessel function which is simply the average of the first and second forms of the Hankel function, so at the origin we avoid a singularity of the EM field.

We can if we want further restrict the incident beam by applying setting the truncation angle to match our microscope object, this essentially applies a cut off point to the In order to compute the scattering from the target particle *ott* uses the t-matrix method, this is not essential for a simple sphere but is far more important for complex shaped particles such as our dimers. If the T-matrix is loaded in from *mstm* we need

to convert the *mstm* t-matrix to a form more suitable for *ott*:

$$\begin{pmatrix} p_{nm} \\ q_{nm} \end{pmatrix} = T \begin{pmatrix} a_{nm} \\ b_{nm} \end{pmatrix} = \begin{pmatrix} aT_{nm}^{TM} & aT_{nm}^{TE} \\ bT_{nm}^{TM} & bT_{nm}^{TE} \end{pmatrix} \begin{pmatrix} a_{nm} \\ b_{nm} \end{pmatrix} \quad (5.2)$$

For *mstm* the T-matrix is packed as a column vector:

$$T_{MSTM} = \begin{bmatrix} aT_{n,-n}^{TE} & bT_{n,-n}^{TE} \\ aT_{n,-n+1}^{TE} & bT_{n,-n+1}^{TE} \\ \dots & \dots \\ aT_{n,n}^{TE} & bT_{n,n}^{TE} \\ \hline bT_{n,-n}^{TM} & bT_{n,-n}^{TM} \end{bmatrix} \quad (5.3)$$

Where as *ott* packs the T-matrix with sub matrices:

$$T_{Ott} = \begin{bmatrix} \begin{pmatrix} aT_{n,-n}^{TM} & aT_{n,-n}^{TE} \\ bT_{n,-n}^{TM} & bT_{n,-n}^{TE} \end{pmatrix} \\ \begin{pmatrix} aT_{n,-n+1}^{TM} & aT_{n,-n+1}^{TE} \\ bT_{n,-n+1}^{TM} & bT_{n,-n+1}^{TE} \end{pmatrix} \\ \dots \\ \begin{pmatrix} aT_{nm}^{TM} & aT_{nm}^{TE} \\ bT_{nm}^{TM} & bT_{nm}^{TE} \end{pmatrix} \end{bmatrix} \quad (5.4)$$

5.1.2 Scattered and Total Fields

With the T-matrix in hand we can compute the scattered beam by multiplying our beam shape coefficients with the T-matrix to get out the scattered field. Now in order to simulate a real QPD we need to account for the motion of our target particle within the trap, taking a typical trajectory file we read off each line in order to translate and

Chapter 5. Detection and Characterisation of rotational spherical aggregate rotational dynamics

rotate the beam. Translation is a rather simple process, simply involving us to shift the beam laterally, small deflections are generally unnoticeable for the incident beam but are much more noticeable in the scattered field (the below figure shows the result of shifting the incident beam $1\mu m$ to the right):

The QPD does not just pick up the scattered light however, it instead is receiving a combined signal from both the incident field and scattered field simultaneously, as mentioned by Rohrbach the total intensity can be computed by taking the magnitude of both the incident field *focused at the origin $[0, 0, 0]$ * and the scattered field originating from $[\delta x, \delta y, \delta z]$ (top left and bottom right plots in the above figure). This means we do not need to worry about any translation effects being 'double-counted' in the QPD's signal as we are only shifting the scattered field meaning the QPD signal is only picking up the interference due to the shifted scattered field. I conducted some unitary tests where I scanned the beam position laterally along the x-axis and measured the QPD's 'x-signal' for x, circular and y-polarized light which yielded the following QPD responses. The target particle was $1.57\mu m$ and the scan range is set to $[-4, 4\mu m]$

Where S_x is given in blue, and S_y is given in orange, the plots make it clear that the polarisation of the beam have a minimal effect on the QPD signals if the particle is traversing in one direction, its clear that the displacement from the beam centre is far more important than the polarization of said beam. This is backed up when we look at Rohrbach's results, who studied a 150 nm sphere ($n = 1.57$) submerged in water with a focusing lens of numerical aperture 1.2, and beam power of 3 mW . The condensing lens' numerical aperture was not set to a particular value and was instead varied between 0.13-1.2, as a compromise we selected a condenser numerical aperture of 0.525, corresponding to a acceptance angle of 31.6° .

Where the points are Rohrbach's results and the solid line's are our QPD's own replication. The dashed horizontal lines on the left represent the maximum displacement in the lateral displacement which is given by the combined beam radius and particle radius (assuming a beam radius of $0.54\mu m$); we can say that any displacements beyond this distance, while non-zero these displacements are unlikely to occur while a particle is trapped at the focus. Whereas the right most plot's dashed horizontal

lines represents the Rayleigh range of the Gaussian beam, this represents the transition between plane wave and spherical wave regimes. Interestingly while our results close to Rohrbach's while close to the focus we see it begins to diverge beyond the first peak, this shouldn't be an issue for a typical optical tweezer calibration as we can assume that the maximum displacement will be within this linear regime.

Now the above plots only consider the QPD response to movements along the cartesian axis, however obviously for any Brownian motion the movements are a combination of displacements in each cartesian direction. We might assume naively that any displacement Δr will result in a linear combination of QPD responses; for low precision force measurements this assumption is adequate, however when high precision is required we find that this assumption is longer adequate due to something referred to as cross-talk. Cross talk arises when movement in one direction results in a QPD response change in the other orthogonal direction, there is no one reason for this effect, it could be a result of differing sensitivity in the photo diodes, it could be because the scattering is slightly asymmetric meaning the scattering falls outside the QPD, or it could be a result of mis-alignment in the set up. This can have unintended effects, for example it may lead to the apparent rise of a curved trajectory rather than a straight path: Consider a particle moving purely along the x-axis, with 0 cross-talk the QPD response should perfectly match the above curve $S_x(x, 0, z_0)$, with S_y being flat in comparison; if however there is cross talk between the channels then S_y will have some significant non-zero value (or it may even grow with increasing displacement), implying that the particle is actually moving in both the x and y directions simultaneously. First we checked for this by measuring the QPD response for random positions within the XY plane:

Where S_x is plotted on top and S_y is plotted below, as shown by the above plot we see that they still possess similar shapes to the previous plots but now with additional noise terms, making it clear that for any trajectory there will be cross talk. This means that trying to get a one-to-one measurement of the particle's displacement is not possible by simply looking at the QPD response, to do that we can need to calibrate the trap.

Berg and Flyvbjerg have an excellent breakdown for accurately calibrating an optical tweezer, in addition they discuss how to minimise cross-talk effects. For two correlated power spectra, the cross correlation is given as:

$$P_x = |\hat{S}_x(f)|^2 \quad (5.5)$$

$$P_y = |\hat{S}_y(f)|^2 \quad (5.6)$$

$$\rightarrow P_{xy} = \text{Re}(\hat{S}_x \hat{S}_y^*) \quad (5.7)$$

Now if the two directions are correlated then $|P_{xy}|^2/P_x P_y$ should be non-zero for all frequencies, in order to eliminate cross-talk effects we need to minimise the cross-correlation for all frequencies. They showed that it is possible to find a transformation of the time series $(x(t), y(t))$ to one that possesses the property that $P_{x'y'}(f) = 0$ for all frequencies. They found these transformed positions by minimising the sum cross-correlation:

$$\sum \frac{P_{x'y'}}{P_x P_y} = \sum \frac{(1 + bc)P_{xy} + cP_x + bP_y}{(P_x + 2bP_{xy} + b^2P_y)(P_y + 2cP_{xy} + c^2P_y)} \quad (5.8)$$

Where b and c are fitting parameters, by minimising this function one can adjust each spectra in order to eliminate cross talk effects and provide a more accurate calibration of the optical trap. Furthermore with the fitting completed, the time series can be then transformed in order to eliminate the cross talk effects:

$$x'(t) = S_x(t) + bS_y(t), \quad y'(t) = S_y(t) + cS_x(t) \quad (5.9)$$

Where x' and y' are now uncoupled coordinates that when Fourier transformed provide the uncorrelated power spectrum. With the fitting complete we can now adjust our time series in order to get a replication of the lateral trajectory.

5.2 Rotations and Asymmetric particles

Rotational motion is something that is not often necessarily considered when characterising Brownian motion, often because separating the contributions from rotational and translational motion is challenging. Depending on the rotational and translational trap stiffness the collected QPD signal will be aliased and typical calibration techniques cannot characterise the particle and trap interactions. This is often why most of the research into trapping asymmetric objects does not delve into power spectra analysis, as there is no real way of modelling the QPD response from an asymmetric object.

Now for isotropic scatterers any rotation is often not an issue when it comes to QPD analysis, even if a sphere rotates 180° the scattering should be identical (assuming its relative position is the same). Now *ott* deals with both translations and rotations by moving the beam itself and computing the scattering from by once again expanding the spherical wave functions, the problem that arises from this is that the portion of the spherical wave that is evaluated by the QPD will pick up said rotation and produce a non-zero signal even if the scatterer in question is isotropic. This means we need to counter rotate the total field prior to collecting the QPD signal, this captures the effects of an anisotropic scatterer but has no effect for an isotropic scatterer. As a test the QPD response from an isotropic sphere of $1.57 \mu m$ was collected at multiple angles, between 0 and 2π , then as a comparison a symmetrical and 1:2 dimer were also subjected to the same rotations and their QPD responses evaluated.

Where on the left we have an isotropic sphere, then a symmetrical dimer, and lastly a 1:2 dimer. The left most plot shows that simply using the inverted rotation matrix is sufficient to prevent rotation effects being double counted. For dimers however, rotating about a given axis gives us a clear change in the signal for even a slight rotation about any axis.

5.3 Power Spectra of single sphere vs spherical aggregates

In order to verify that the QPD is outputting correct signals we first compared the module to the only other known instance of simulating a QPD response, that being

Chapter 5. Detection and Characterisation of rotational spherical aggregate rotational dynamics

the work of [Rorhbach](#). In their paper they looked at the signal response produced by a single sphere ($r = 150 \text{ nm}$, $n = 1.57$) being scanned along the three Cartesian axis in the proximity of a 1064 nm NIR beam with a numerical aperture of 1.2. As shown by fig ?? the two responses are remarkably accurate close to the origin; with only slight deviations as you move past the harmonic region, the difference can be explained due to how the two evaluate the total fields. Where in our case the incident and scattered fields are reduced to 0 at the origin, whereas Rohrbach’s work evaluates the fields the fields as being non-zero at all points, as you move beyond the origin this discrepancy grows.

Since we are only interested in the dynamics of spherical aggregates upon reaching equilibrium we do not need to be concerned about the deviation from Rohrbach’s results so long as the particle’s displacement does not exceed the linear region at the origin. The axial response curve is slightly more involved, requiring that the condenser lens numerical aperture is adjusted until a harmonic response curve is achieved [4].

In order to verify that the QPD can accurately capture the dynamics of the target particle we first simulated a single sphere ($a = 1 \mu \text{ m}$, $n = 1.59$) in the focus of a 1064 nm laser. Using *ott* the trap stiffness is computed by applying a linear fit to the force-displacement curve along the x and y axis; for a linearly polarised trap the gradient force is greater in the polarisation direction than transverse case. We see this reflected in the simulated QPD, the fitted Lorentzian curves have different corner frequencies indicating that the beam’s polarisation is influencing the dynamics of the trap.

Next we consider a dimer composed of two sphere’s similar to the previous sphere, we again apply the QPD module to reproduce the power spectrum. Previous experimental work found that a pair of trapped beads would half the corner frequency from the reported power spectra. However, in our own simulations we see instead an increase in the expected trapping force from our QPD method, with the maximum trap stiffness expected for a dimer of size ratio 5. Compared to *ott* in which the maximum trapping strength is expected at a size ratio of 2. This can be somewhat explained by the fact that as the second sphere shrinks the centre of diffusion approaches the centre of the

Chapter 5. Detection and Characterisation of rotational spherical aggregate rotational dynamics

larger sphere and thus the dimer’s orientational behaviour is similar to a single sphere, only subject to slight Brownian motion. Therefore one should expect that for aggregates containing multiple sized particles (e.g. cellular samples) typical characterisation techniques may over estimate the strength of the trap.

5.4 Monitoring Stochastic rotational motion using static light scattering

Orientalional dynamics to an anisotropically scattering shape are difficult to characterise due to the coupling of rotational and translational effects. As shown in the previous chapter the dynamics of even simple dimers are heavily dependent on the particle’s position and orientation, this is reflected in literature where several engineering solutions have been devised to decouple translational and orientational motion [,]. While a majority of latter work has been focused on nano-particles (falling into the Rayleigh Regime) and utilising florescence

5.4.1 Coordinate System

In the case of our probe beam the +z direction points from the surface of the probe directly to the centre of diffusion in our dimer, with the +y direction pointing towards what would be our trapping beam, and the +x direction pointing into the page. The origin of our coordinate system is fixed on the centre of the focus of our trapping beam, meaning as our dimer’s centre of diffusion moves the origin is kept constant.

5.4.2 Beam

The probe is a defined as a plane wave by setting the Gaussian beam parameter C_B to 0. We also say the beam is un-polarized by defining the Stokes vector as $[1, 0, 0, 0]$. The plane wave in *mstm* is given by (??).

5.4.3 Dimer

The dimer is defined by two spheres, in the trapping frame this would be orientated by $s = [0, 0, 1]$ however in our scattering set up this is rotated to $s = [-1, 0, 0]$ as the large sphere is furthest from the trapping beam. We scale the position of each sphere by the factor L :

$$L = \frac{1}{k} = \frac{\lambda}{2\pi} \quad (5.10)$$

Where λ is the wavelength of light and is given in nanometres, this means every position must be also provided in nanometres.

5.4.4 Detectors and Pixels

Each detector is placed roughly $2 \times 10^5 nm$ from the dimer (can be adjusted later for testing), with the position of the detector being defined by the polar and azimuth angles (θ & ϕ respectively) such that:

$$[x_{fiber}, y_{fiber}, z_{fiber}] = [rcos(\phi)sin(\theta), rsin(\phi)sin(\theta), rcos(\theta)] \quad (5.11)$$

So if you were to place the fibres in the trapping frames x-y plane (i.e. flat against the cover slip in a covenantal trapping context), in the probe beam frame will only have x and z components. The orientation of the detector is just the -ve of its position and not scaled by the distance term r , the orientation being the vector from the origin of the detector to the center of the dimer.

Pixels can be thought of as points lying on the surface of the detector, by getting the spherical coordinates of each pixel we can compute the intensity at each point on the detector, allowing us to determine the average intensity on a given detector.

Where each point is first scaled to the size of the detector - for now we assume a radius of $2.5 \times 10^4 nm$ - and then translated from its position on the surface of the detector to the main coordinate system. Their orientation is treated much in the same as the detector's orientation, being its -ve position and scaled down by the radial

distance from the dimer to the pixel, making it a unit vector. From their position we can also grab their spherical coordinates to create a list of points for *mstm* to evaluate. In order to accurately describe any detector surface we can use a Householder transformation to get the perpendicular circular surface of any vector.

This allows us to define the surface of any detector perpendicular to the origin of our coordinate system, we can freely choose the size and resolution of our fibre's. For every pixel we define the spherical coordinates relative to our origin, this is added to a list of θ, ϕ pairs that are evaluated by *mstm*.

5.5 Interpretation of scattering data into orientation estimates

Consider a dimer in the optical trap (Fig. 5.1a), we can define at any point in time a unit vector \hat{s} pointing from the centre of the larger sphere to the centre of the smaller sphere. A plane wave probe beam is incident on the trapping laser, is incident on the dimer, generating a scattering pattern dependent on the dimer's orientation $I(\hat{s}, \theta, \phi)$ which can be computed using *mstm* [5]. To represent the experimental set up consisting of a set of optical fibres recording scattered light, we choose four sets of spherical angles $[(\theta_1, \phi_1), (\theta_2, \phi_2), (\theta_3, \phi_3), (\theta_4, \phi_4)]$ and record the calculated intensity at each angle $I(\hat{s}, \theta_k, \phi_k)$.

Our goal is to determine the orientation of the trapped dimer based on the measured intensity $I(\hat{n}, \theta_k)$. Rather than aim immediately for an exact estimate of the dimer's orientation, for the purposes of interpretation of the scattering and optimisation of the measurement setup it is more convenient to discretize the possible orientation space into a number of possible reference orientations, which we can then use as 'classification categories' in a neural network methodology to map scattering data to orientation (see below for further discussion). Here we choose $n_{ref} = 30$ reference orientations $\hat{\mathbf{n}}_\alpha$ evenly distributed on a unit sphere [6] (Figure 5.1b) leading to a maximum nearest-neighbour spacing between two neighbouring reference orientations of 0.895 radians. Using MSTM we compute the raw intensities at each of the measurement angles that

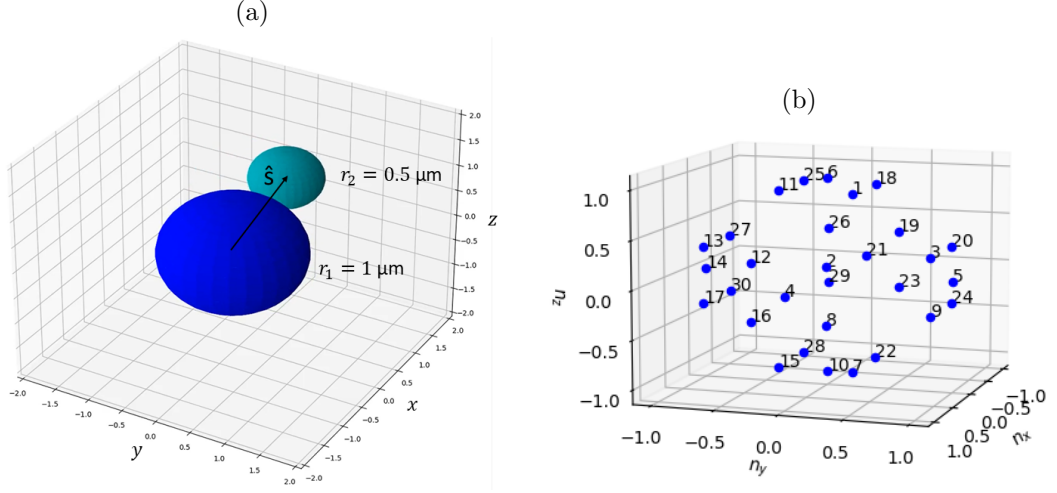


Figure 5.1: (a) Example dimer in orientation $\hat{\mathbf{s}}$, (b) 30 Reference orientations represented by vectors pointing from $[0,0,0]$ to each point

would be generated by a dimer in each reference orientation, $I(\hat{\mathbf{n}}_\alpha, \theta_k)$. While the number and position of detection fibres is technically arbitrary there are several constraining factors that limit our ability to infer useful information from the trapped object, see Section ?? for a detailed breakdown of our choice of detection angles. The raw intensities are normalized according to:

$$y_k(\hat{\mathbf{n}}_\alpha) = \frac{I(\hat{\mathbf{n}}_\alpha, \theta_k) - \langle I(\hat{\mathbf{n}}, \theta_k) \rangle}{\langle I^2(\hat{\mathbf{n}}, \theta_k) \rangle - \langle I(\hat{\mathbf{n}}, \theta_k) \rangle^2} \quad (5.12)$$

where the denominator is simply the standard deviation across the set of values $I(\hat{\mathbf{n}}, \theta_k)$. The reference orientations, raw intensities, and scaled signals are given in Tables ?? and ??.

Note that the collected scattering signals are not necessarily simply related to their associated reference orientations: as is well known from such examples of the inverse scattering problem. While it is trivial to compute the light scattering pattern for any given particle with any particular characteristic (i.e. size, shape, or orientation), inferring the light scattering from a unknown particle to determine said characteristic is incredibly difficult due to complex mapping between scattering and said characteristic. Even if the orientation space is divided evenly between reference orientation the subse-

Chapter 5. Detection and Characterisation of rotational spherical aggregate rotational dynamics

quent signal space ends up being appearing mixed making simple comparisons of signals useless for inferring information on the particle. Shown below is two clusters of orientation vectors and there respective measured scattering signals - the points have been coloured based on their proximity to the centre of their respective cluster. While the orientation space appears tightly packed and ordered the signal space quickly spreads out in an asymmetric fashion. Furthermore as seen in Fig 5.2b the signal mapping can intersect itself which only further increases the complexity. While in some instances the mapping between one reference orientation and another is discrete, in other instances the mapping becomes far more complex to discern.

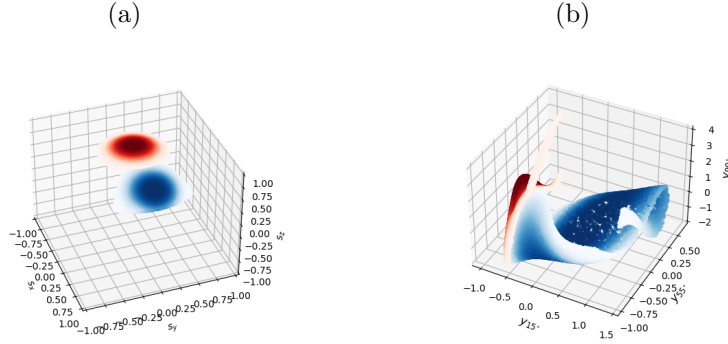


Figure 5.2: (a) Distribution of orientation vectors and (b) their respective scattering signals. Points are coloured according to their distance from the centre of each cluster (red points centred around $[0.00, 0.00, 1.00]$, blue points centred at $[0.71, 0.00, 0.71]$)

Nevertheless, at least where the uncertainty in signal measurements is low (see below), we can predict the orientation from the scattering by utilising computational techniques such as neural networks. We thus utilised the Python machine learning program *scikit-learn* [7] to build a neural network for identifying the dimer's orientation from its light scattering signal. The network was trained by generating a database of random orientation vectors, calculating the corresponding light scattering signals, and then using the network to estimate the probability of a given signal coming from a dimer in a given reference orientation. The network's loss function was evaluated and used to improve the estimation, the network being trained until the improvement in the loss function was less than 0.0001.

Importantly, the estimation provided by the neural network can be improved further by accounting for any prior information we know about the dimer, utilising Bayesian inference to update the neural network’s estimation:

$$p(\hat{\mathbf{n}}_\alpha | y_k(\hat{\mathbf{s}})) = \frac{p(y_k(\hat{\mathbf{s}}) | \hat{\mathbf{n}}_\alpha) p(\hat{\mathbf{n}}_\alpha)}{p(y_k(\hat{\mathbf{s}}))} \quad (5.13)$$

where $p(\hat{\mathbf{n}}_\alpha)$ and $p(y_1, y_2, y_3)$ are the prior estimates of the distributions of particle orientations and instantaneous signals, respectively. *Without* any prior evidence we must assume that the orientation prior of the dimer $p(\hat{\mathbf{n}}_\alpha)$ is uniform. However, inference about the dimer’s possible current orientation from knowledge of previous measurements can be used to inform our estimate of $p(\hat{\mathbf{n}}_\alpha)$. The latter prior $p(y)$ is the probability of measuring a signal (y_1, y_2, y_3) . This is given by taking the discrete integral over the collection of reference orientations:

$$p(y_1, y_2, y_3, y_4) = \sum_{\alpha=1}^{n_{\text{ref}}} p(y_1, y_2, y_3, y_4 | \hat{\mathbf{n}}_\alpha) p(\hat{\mathbf{n}}_\alpha) \quad (5.14)$$

From (5.13) we obtain the key result, a mass probability distribution denoting the probability that our dimer is in orientation $\hat{\mathbf{n}}_\alpha$ given a measured signal (y_1, y_2, y_3) , *i.e.* an estimated mapping from scattering measurement to orientation estimate.

5.5.1 Calculation of error

To evaluate the above estimation of dimer orientation from scattering signal, we use a Brownian simulation of a dimer in the optical trap (Section 5.5.2) to compare estimated most probable reference orientation, derived from the dimer’s scattering through Eq. (5.13), with the dimer’s known *actual* orientation $\hat{\mathbf{s}}$. MSTM provides calculated light scattering from the simulated dimer $I(\hat{\mathbf{s}}, \theta)$ and we use (5.12) to obtain normalized values at each measurement angle θ_k , $y_1(\hat{\mathbf{s}})$, $y_2(\hat{\mathbf{s}})$, $y_3(\hat{\mathbf{s}})$, from which we obtain $p(\hat{\mathbf{n}}_\alpha \parallel y_1, y_2, y_3)$. Because we know the actual orientation $\hat{\mathbf{s}}$ we can measure the error in the model’s estimate by comparing the reference orientation closest to $\hat{\mathbf{s}}$, denoted as $\hat{\mathbf{n}}_{\text{best}}$, with the most probable predicted orientation from Eq. (5.13). An ideal result

would be one where the probability distribution is 0 for every $\hat{\mathbf{n}}$ apart from $\hat{\mathbf{n}}_{best}$:

$$p_{best} = \begin{cases} 1 & \text{when } \hat{\mathbf{n}}_\alpha = \hat{\mathbf{n}}_{best} \\ 0 & \text{anywhere else} \end{cases} \quad (5.15)$$

In reality the distribution from Eq. (5.13) will assign some non-zero probability to every reference orientation, leading to some level 'confidence' in orientation prediction, which can be quantified by calculating the Kullback-Leibler divergence K_l between the two distributions:

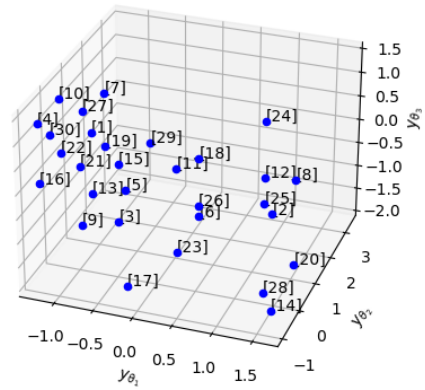
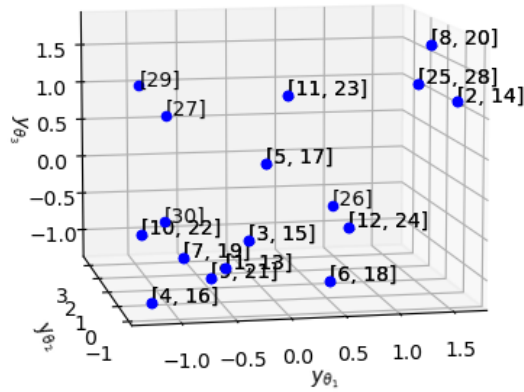
$$K_{l,\#}(p_{best} \parallel p(\hat{\mathbf{n}}_\alpha|y_1, y_2, y_3)) = p_{best} \ln \left[\frac{p_{best}}{p(\hat{\mathbf{n}}_{best}|y_1, y_2, y_3)} \right] \quad (5.16)$$

where a larger value of K_l indicates that our model is less confident in its prediction of the dimer's orientation. The divergence K_l thus illustrates the 'spread' in the estimated dimer orientation probability — a distribution strongly peaked at some value would give us more confidence in that value than a near-uniform distribution where the scattering measurement could imply a wide range of possible orientations — but it does not directly indicate our estimates actual accuracy, that can be simply defined as the percentage of our estimations that are correct.

5.5.2 Brownian Simulation

We use the Brownian OT package developed by Fung *et al* [?] to simulate the motion of an asymmetric dimer (Figure 5.1a) within an optical trap. Brownian OT combines MSTM [?] and “Optical Tweezer Toolbox” (*ott*) [8] to simulate the motion of arbitrary shaped sphere clusters. We simulate the motion of a dimer trapped in a highly focused Gaussian beam by calculating the optical forces imparted by the laser, and the Brownian force due to the surrounding fluid. MSTM provides the necessary T-matrix to compute the optical force via *ott*. The Brownian force is found by computing the dimer's diffusion tensor according to the analytical solutions provided by Nir and Acrivos [?]. We simulated a polystyrene dimer ($n = 1.59$) in a suspension of water ($n_{med} = 1.33$) over the course of 1 s with a simulation time step of 1×10^{-5} s. We

placed the dimer 4 microns below the trap focus at an angle 30° from the horizontal, the resulting trajectory is shown below in Sec 5.5.4. We chose these initial parameters because it demonstrates our model's performance in non steady state conditions.



given signal to a particular parameter value.

To remedy this we raise the third detector out of the x-y plane; as such the expected signals from each reference orientation is unique. As seen between Figures 5.3a & b each reference orientation now has a unique scattering signal, though with only three detectors the difference in expected signals can appear insignificant. By adding a 4th detector we can differentiate signals more reliably, improving the neural networks performance. In line with our goal of making this method viable in a laboratory setting we decided not to increase the number of detectors further than 4.

5.5.3 Testing the Model

Using our simulation from Section 5.5.2 we simulated the motion of a silica dimer ($n = 1.45$) trapped in water ($n = 1.33$) within a 5 mW optical trap. The trapping laser is 1064nm NIR focused through a 1.25 NA objective. The dimer is comprised of two tangent spheres with radii $1\mu m$ and $0.5\mu m$ respectively. We simulated the first 10 seconds of motion, calculating the orientation and position every 1 ms.

We applied Eq. (5.13), taking the reference orientation with the highest probability as our estimate of the dimer's instantaneous orientation $\hat{\mathbf{n}}_{est}$. To visualise the model's performance we plotted the radial distance between our estimation $\hat{\mathbf{n}}_{est}$ and the dimer's *actual* instantaneous orientation $\hat{\mathbf{s}}$ versus time. For comparison, we also plotted the radian distance between the dimer's instantaneous orientation and the closest reference orientation, denoted $\hat{\mathbf{n}}_{best}$. The dotted line indicates the maximum radian distance (0.896 radians) between two *neighbouring* reference orientations: if we are under this line then we know our estimate is at least neighbouring the best result. Assuming a uniform prior of the reference orientations $p(\hat{\mathbf{n}}_\alpha)$ the neural network's predictions ($\hat{\mathbf{n}}_{est}$ from Eq. (5.13)) are at times reasonable, but there are significant large and random jumps away from the correct result (Fig. 5.4).

One reason we observe such large jumps in orientation estimated from scattering signals is that there is no simple correlation between the 'distance in scattering space' between scattering signals from two different orientations, and their separation in orientation space: even a large change in orientation can involve a small change in scattering.

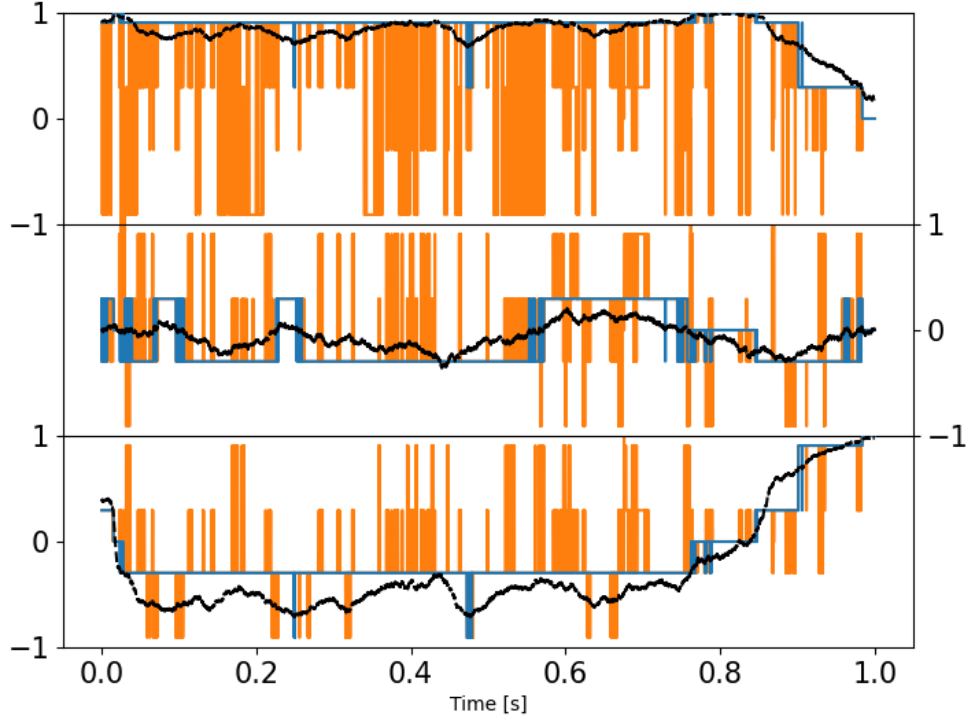


Figure 5.4: Model's estimation of dimer orientation over the simulation time, assuming uniform prior $p(\hat{\mathbf{n}}_\alpha)$, broken up into x, y, and z components for clarity. Blue line denotes the best result we can achieve (the reference orientation $\hat{\mathbf{n}}_{best}$ that is closest to the actual orientation), orange line denotes the result provided by eq 5.13: where the orange line is not visible, the model's prediction agrees with $\hat{\mathbf{n}}_{best}$. Dotted black line is the instantaneous orientation $\hat{\mathbf{s}}$.

Combining this fact with use of a uniform prior, indicating essentially no knowledge of how orientation should behave, there is no constraint on how much estimated orientation can change from time-step to time-step. To improve the estimation we can therefore use knowledge of the physical limitations of the object in the trap and its dynamics, imposing a more physically grounded prior, accounting in this case for the fact that the motion of the dimer is limited due to the trap stiffness. Here the prior of the reference orientations $p(\hat{\mathbf{n}}_\alpha)$ was redefined at each time step as a Boltzmann distribution of the physical distance between the previous estimate $\hat{\mathbf{n}}_{est}(t - \Delta t)$ and each reference orientation $\hat{\mathbf{n}}_\alpha$. Put simply, we are reweighing our estimation based on the

size of rotation required, with smaller movements being favoured over large movements:

$$p(\hat{\mathbf{n}}_\alpha) = \frac{e^{\beta(\hat{\mathbf{n}}_\alpha \cdot \hat{\mathbf{n}}_{est}(t-\Delta t))}}{\sum_{\alpha=1}^{n_{\text{ref}}} e^{\beta(\hat{\mathbf{n}}_\alpha \cdot \hat{\mathbf{n}}_{est}(t-\Delta t))}} \quad (5.17)$$

Here β is a weighting factor describing the dimer's freedom of motion within the trap. As shown in Figure 5.5 implementation of Eq (5.17) helps significantly reduce the large random excursions of estimated orientation away from the 'best' result.

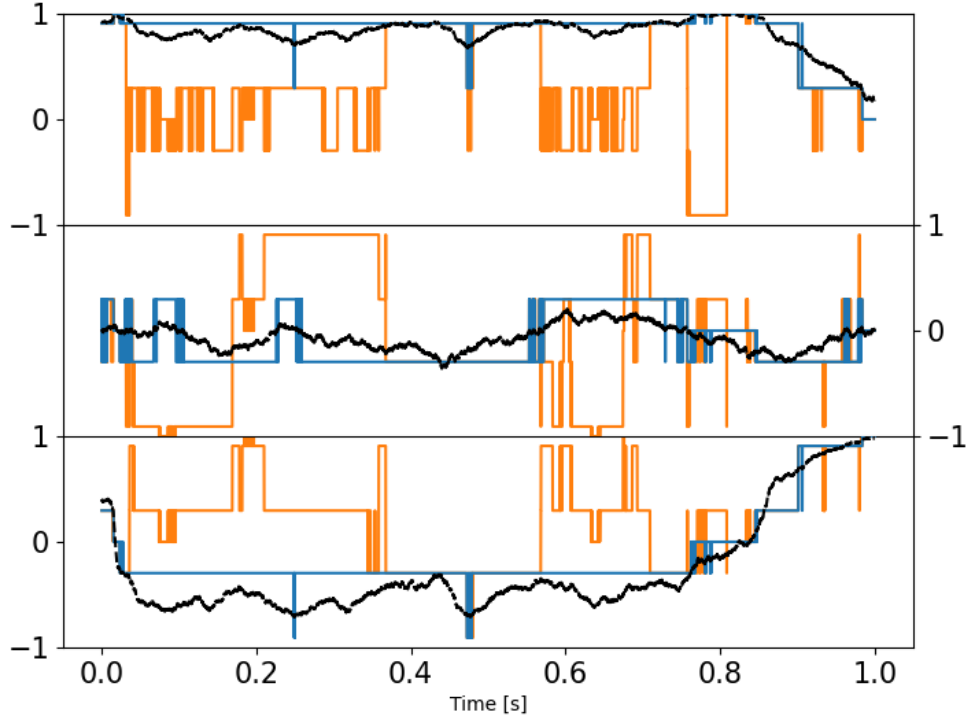


Figure 5.5: Estimation of dimer orientation with $p(\hat{\mathbf{n}}_\alpha)$ defined by Eq (5.17). Blue line denotes the best result we can achieve, orange line denotes the result provided by eq 5.13. Dotted black line is the instantaneous orientation $\hat{\mathbf{s}}$ (see Section ??).

The simulation data from Section 5.5.2 was used to evaluate our model's performance — covered in Section 5.5.1. By summing the divergence of each measurement across the entire simulation we get an evaluation of how well the model performed in estimating the dimer's orientation. To compare the effects of changing certain param-

eters on the performance of our model we compare our result of $K_{l,total}$ to a worst case scenario and evaluate how much it improves upon this, denoted as $F(K_l)$:

$$K_{l, total} = \sum_{\# = 1}^{timesteps} K_{l, \#} \quad (5.18)$$

$$K_{l, worst} = \sum_{\# = 1}^{timesteps} \ln \left[\frac{1}{1/n_{ref}} \right] \quad (5.19)$$

$$F(K_l) = \frac{K_{l, worst}}{K_{l, total}} \quad (5.20)$$

The worst case scenario is akin to randomly choosing a reference orientation at each time step. The greater the value of $F(K_l)$, the better our model's confidence is in characterising the dimer's motion. Because our model is dependent on several parameters we need to a sophisticated method for understanding how these parameters correlate with $F(K_l)$.

5.5.4 Asymmetric dimer dynamics

A simulation of a ($a_1 = 1 \mu\text{m}$, $a_2 = 0.5 \mu\text{m}$) over the first 1 seconds of entering the optical trap. The initial orientation was set at $s = (0.923, 0.0, 0.385)$. The dimer's position and orientation was recorded every $10 \mu\text{s}$ for using as a test dataset for our model.

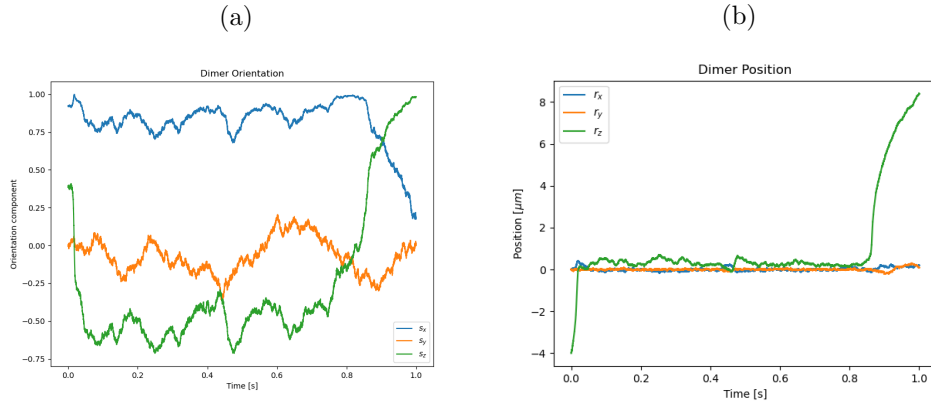


Figure 5.6: Simulation results of: (a) the dimer's orientation vector with time, (b) the dimer's $[x,y,z]$ position with time.

In the simulations of Vigilante *et al.* [?], trapped symmetrical dimers were investigated; their findings showed that the optical torque on the dimer goes to zero while aligned vertically and is at its maximum in a horizontal alignment. However as seen in Figure 5.6 asymmetric dimers demonstrate dynamics that do not immediately achieve steady state. We chose to use asymmetric dimers as our benchmark due to this fact, as its orientational motion is far more complex than a symmetric dimer. In the future we hope to further investigate the motion of asymmetric dimers.

5.5.5 Accounting for sources of error in light scattering measurements

When it comes to analysing light scattering from any size particle, error analysis becomes a significant factor. Typically this can be accounted for by averaging over long periods of time to get an assessment of the steady state conditions of the target particle. However in our case where we wish to know the instantaneous orientation, we instead have to rely on our understanding of how uncertainty can effect our model's performance. We identified two areas which are likely sources of error in our estimation: firstly, an incorrect modelling of the target particle, and secondly, signal noise arising from experimental factors. We highlight how we address these areas below.

Impact of incorrect dimer sizing One of the main limitations of our model is that we assume that the dimer being modelled in MSTM is accurate to the dimer being trapped in the optical tweezer. Sizing molecules accurately is a significant challenge for single particle analysis so there is bound to be some uncertainty with the measurements. We ran our model 3 times with the neural net being trained on a dimer of size ratio 1 : 1.95, 1 : 2.00 and 1 : 2.05.

As can be seen from Fig 5.7 even the slightest change in size ratio makes a very significant difference to the performance of our model. This amounts to just over 100 *nm* in the dimer's overall size, yet results in our model being correct from over 90 % of the time to now as low as 30 %. This highlights the importance of correctly sizing trapped entities before performing any in depth analysis of the scattering pattern, as even the slightest deviation can have a serious impact. We addressed this by increasing the

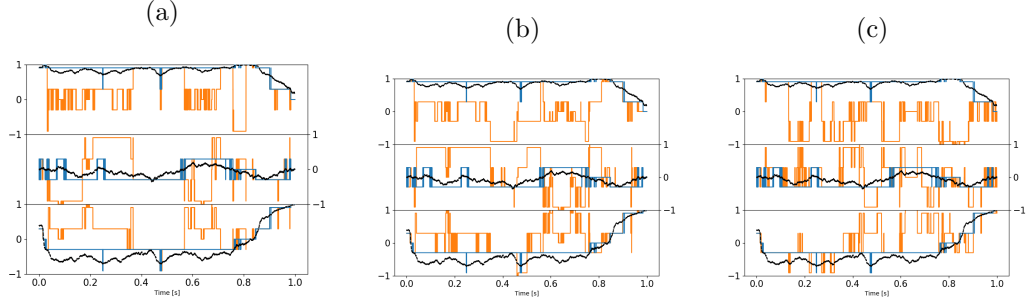


Figure 5.7: Model estimates of orientation when neural net has been trained on dimer of size ratio: (a) 1:2 [$F(K_l) = 9.456$], (b) 1:2.05 [$F(K_l) = 1.324$], (c) 1:1.95 [$F(K_l) = 1.325$] ($n_{refs} = 30$)

number of available reference orientations from 30 to 126 (following the same procedure as given by [?] to evenly space out the coordinates) and increasing the weighting factor in Eq 5.17. While this didn't have a significant improvement on the overall accuracy of the model, in the worst case having a slight increase from 30.5 % to 40.3 %, it did help to significantly reduce the magnitude between our model's estimations and the dimer's motion as seen below in Fig 5.8.

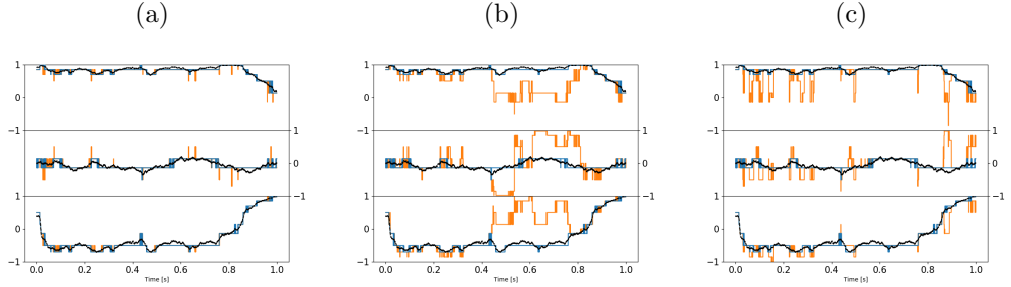


Figure 5.8: Model estimates of orientation when neural net has been trained on dimer of size ratio: (a) 1:2 [$F(K_l) = 11.756$], (b) 1:2.05 [$F(K_l) = 1.233$], (c) 1:1.95 [$F(K_l) = 2.128$], ($n_{refs} = 126$)

Notably the increasing the number of reference orientations had a greater effect when our neural network was trained on a 1:1.95 dimer than a 1:2.05 dimer. This suggests that overshooting our size estimate will be less detrimental to our estimation. Notably if the our sizing is off the neural network does not predict a smooth motion within the trap; instead predicting that the dimer is jumping back and forth between

different orientations. This suggest that we can narrow down our estimate of the particle's size by assessing how the dimer is reorienting within the trap, as we should expect a smooth continuos prediction. Since we are working with a spherical dimer it also stands to reason that techniques such as image analysis could be used in part to address this, so long as the trapped entity is sufficiently illuminated.

Impact of measurement noise on model predictions So far a key assumption of the neural network implementation is that the detected scattering signal has no uncertainty associated with it. In reality of course scattering signals will always have some non-zero measurement noise. This can be attributed to a variety of factors, from a measurement bias in the detector, to the Brownian motion of the dimer itself. To explore the impact of measurement uncertainty on orientation estimation model performance we introduce a Gaussian noise to the measured signal:

$$I(\hat{\mathbf{s}}) = I(\hat{\mathbf{s}}) \pm \epsilon I(\hat{\mathbf{s}}) \quad (5.21)$$

where ϵ is the percentage error associated with the scattering signal. Figure 5.9 shows the performance of the model at a range of ϵ using in-plane detector angles 15° , 55° , 90° and out-of-plane detector at 75° , with β set to 1:

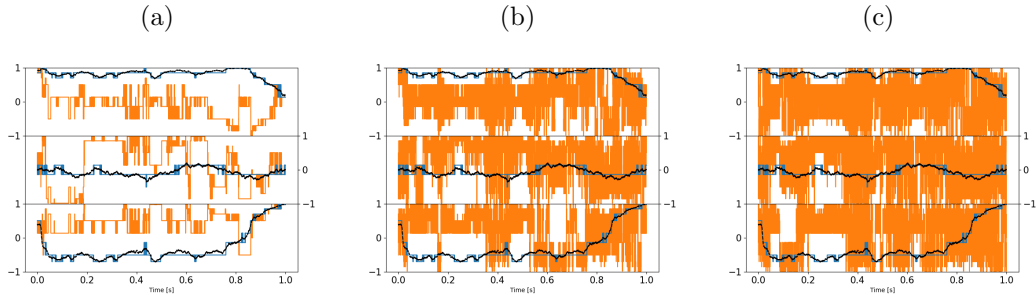


Figure 5.9: Model prediction for signal error of (a) 1% $[F(K_l) = 7.246]$, (b) 15% $[F(K_l) = 0.511]$, and (c) 25% $[F(K_l) = 0.536]$.

As can be seen from Figure 5.9, the inclusion of signal noise quickly leads to a decrease in the model's performance. This is due to an inherent feature of the inverse scattering problem: two distinct regions in orientation space can become heavily inter-

twined and thus no longer well separated when mapped to intensity space (even though the mapping remains continuous): so even small uncertainties in the scattering data can lead to large 'mistakes' in the choice of orientation by the neural network. (Indeed if this was not the case the inverse scattering problem would be quite simple.)

To reduce the effects of the signal noise we took the time average of the expected signal over 0.001s and then had our neural network estimate the orientation based on the average signal.

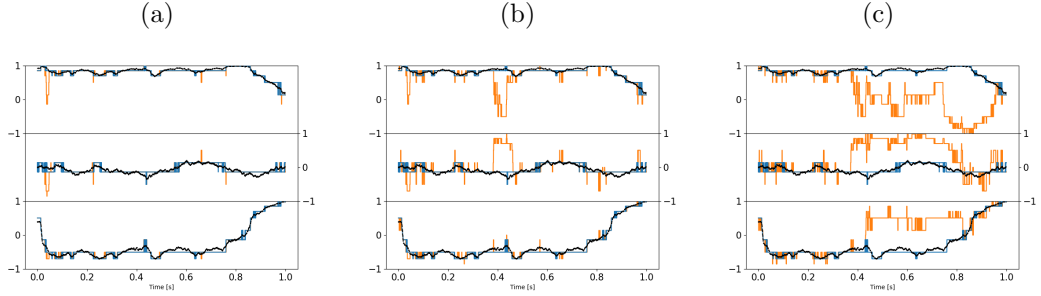


Figure 5.10: Model prediction for signal error of (a) 1% [$F(K_l) = 4.823$], (b) 15% [$F(K_l) = 1.494$], and (c) 25% [$F(K_l) = 0.882$], time averaged over 1 ms

This resulted in a reduction in the overall signal noise and provided a higher degree of accuracy for our model. There appears to be no clear correlation between the length over which we time average and the performance of our model. Time averaging over every 0.05s resulted in a drastically worse performance; this is due to the fact that over longer time periods there is greater uncertainty regarding how the dimer's orientation has changed, thus tracking the instantaneous orientation becomes harder for the neural network. Fortunately, time averaging even over 1 ms seems to provide a satisfactory estimation of the dimer's angular dynamics within the optical trap.

From the above discussion it's clear that estimation of the dimer's orientation is a problem that can be endlessly tuned to fully maximise our end result. Here we simplify the problem somewhat by employing a relatively small finite number of 'reference orientations' to map between scattering and dimer orientation: the precision of estimation could be improved by utilising a greater number of reference orientations, although there remains a balance between the realisable precision of orientation estimate and the

noise level of the scattering measurement. Another avenue to further explore would be using the method to optimise the choice of detection angles, essentially to find the region in the mapping between measured scattering and orientation that offers the best degree of confidence through optimal separation of scattering signals for distinct orientations. For sequences of data such as dynamic measurements, a further potential enhancement would be to consider more complex correlations based on prior expectations of the dynamics. Here already we improve the method using a non-uniform prior based on only the immediately previous measurement in time (see Section 2.1): considering a non-uniform grouping of reference orientations might result in a better estimation, if we have information regarding the dimer’s preferred axis of rotation.

5.6 Conclusion

We have developed a method for measuring the dynamics of an optically-trapped colloidal objects based purely on measurements of the object’s light scattering at a small number of detection angles. We demonstrate the method using the orientation of an asymmetric dimer as the dynamic variable and object of interest respectively, but in principle the model can be applied to any characteristic that impacts the light scattering pattern produced by a trapped entity such as size and shape. The MSTM package is a flexible tool for calculating the light scattering of complex objects using a representation of the object as a set of micro-particles, enabling training of a neural network to enable categorisation of the mapping between scattering and trapped object characteristics. By taking account of the physically realistic behaviour of the trapped object and the characteristics of the trap (which impact the dynamics of the object), the Bayesian inference method can be refined to provide a reliable estimation of object characteristics of interest, even in the presence of measurement noise. Fundamentally, the inverse scattering problem is difficult to solve, since the mapping between object characteristics and scattering can be highly complex. We determined the minimum number of detectors required for a reliable estimation in the presence of measurement noise; furthermore, we demonstrated that the arrangement of these detectors is critical

Chapter 5. Detection and Characterisation of rotational spherical aggregate rotational dynamics

for a reliable estimation of an objects orientation. However, Bayesian inference based on neural network estimation of the mapping provides a powerful method for practical applications, extending the use of optical trapping beyond measuring microscopic force response toward detailed structural and dynamic information about complex trapped entities.

Bibliography

- [1] Yogesha, S. Bhattacharya, and S. Ananthamurthy, “Precise characterization of micro rotors in optical tweezers,” *arXiv: Soft Condensed Matter*, 2011. [Online]. Available: <https://api.semanticscholar.org/CorpusID:118262469>
- [2] R. Bar-Ziv, A. Meller, T. Tlusty, E. Moses, J. Stavans, and S. A. Safran, “Localized dynamic light scattering: Probing single particle dynamics at the nanoscale,” *Physical Review Letters*, vol. 78, no. 1, p. 154–157, Jan 1997.
- [3] A. Meller, R. Bar-Ziv, T. Tlusty, E. Moses, J. Stavans, and S. Safran, “Localized dynamic light scattering: A new approach to dynamic measurements in optical microscopy,” *Biophysical Journal*, vol. 74, no. 3, pp. 1541–1548, Mar. 1998.
- [4] L. Friedrich and A. Rohrbach, “Tuning the detection sensitivity: a model for axial backfocal plane interferometric tracking,” *Opt. Lett.*, vol. 37, no. 11, pp. 2109–2111, Jun 2012. [Online]. Available: <https://opg.optica.org/ol/abstract.cfm?URI=ol-37-11-2109>
- [5] D. W. Michael I. Mishchenko, Larry D. Travis, “T-matrix computations of light scattering by nonspherical particles: A review,” *Light scattering by Non-Spherical Particles*, vol. 55, pp. 535–575, 1996.
- [6] G. C. Reythor, “Numerical methods for radiative heattransfer,” Doctoral Thesis, Universitat Politècnica de Catalunya, 2006.
- [7] F. Pedregosa, G. Varoquaux, A. Gramfort, V. Michel, B. Thirion, O. Grisel, M. Blondel, P. Prettenhofer, R. Weiss, V. Dubourg, J. Vanderplas, A. Passos,

Bibliography

- D. Cournapeau, M. Brucher, M. Perrot, and E. Duchesnay, “Scikit-learn: Machine learning in Python,” *Journal of Machine Learning Research*, vol. 12, pp. 2825–2830, 2011.
- [8] I. C. D. Lenton, T. A. Nieminen, V. L. Y. Loke, A. B. Stilgoe, Y. Hu, G. Knöner, A. M. Brańczyk, N. R. Heckenberg, and H. Rubinsztein-Dunlop, “Optical tweezers toolbox,” <https://github.com/ilent2/ott>, 2020.